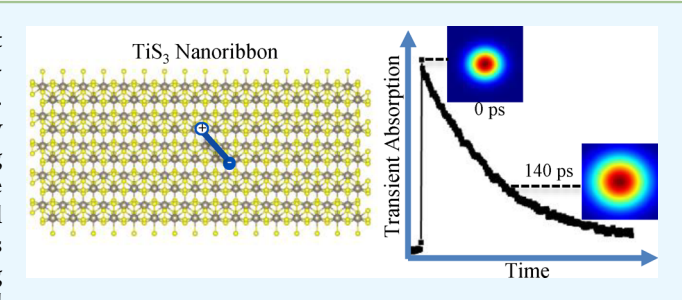


Time-Resolved Measurements of Photocarrier Dynamics in TiS₃ **Nanoribbons**

Qiannan Cui, [†] Alexey Lipatov, [‡] Jamie Samantha Wilt, [†] Matthew Z. Bellus, [†] Xiao Cheng Zeng, [‡] Judy Wu, [†] Alexander Sinitskii.*,‡ and Hui Zhao*,†

Supporting Information

ABSTRACT: We report synthesis and time-resolved transient absorption measurements of TiS3 nanoribbons. TiS3 nanoribbons were fabricated by direct reaction of titanium and sulfur. Dynamics of the photocarriers in these samples were studied by transient absorption measurements. It was found that following ultrafast injection of nonequilibrium and hot photocarriers, the thermalization, energy relaxation, and exciton formation all occur on a subpicosecond time scale. Several key parameters describing the dynamical properties of photocarriers, including their recombination lifetime, diffusion coefficient, mobility, and diffusion length, were deduced.



KEYWORDS: titanium trisulfide, carrier dynamics, nanoribbon, transient absorption, exciton

1. INTRODUCTION

Recently, transition metal dichalcogenides (TMDs) based on Mo and W have drawn considerable interest as new forms of nanomaterials. These two-dimensional (2D) materials have several exotic properties, such as indirect-to-direct band gap transition in monolayers, ^{1,2} valley-selective optical coupling, ^{3–5} large exciton binding energies, ^{6–9} and strong nonlinear optical responses. 10-14 In addition, these atomic sheets can be used as building blocks to fabricate new van der Waals heterostructures 15-17 and multilayers. However, these materials have optical band gaps shorter than 800 nm and are highly sensitive to the thickness. New 2D materials with absorption bands extend to near-infrared range, and direct band gaps in both monolayer and bulk are highly desired in applications such as night vision, thermal imaging, and optical communications. They would also open up new dimensions in van der Waals heterostructures by providing new functionality.

Transition metal trichalcogenides, MX_3 (where M = Ti, Zr, Hf, Nb, Ta and X = S, Se, Te), can offer complementary electronic and optical properties to TMDs but are still largely unexplored. 18 TiS₃ is one of the first members of this material family that started gaining attention due to its low cost production from earth abundant elements. A TiS3 crystal is composed of parallel sheets of chains of stacked triangular prisms that are held by van der Waals forces. Ab initio calculations show that the TiS3 monolayer is a direct-gap semiconductor with a band gap of 1.02 eV119,20 and with an exceptionally high in-plane electron mobility of about 10000 cm² V⁻¹ s⁻¹. ^{19,21} Experimentally, TiS₃ nanoribbons have been

synthesized²²⁻²⁵ and used to fabricate field-effect transistors with room temperature electron mobilities in the range of 1-40 cm² V⁻¹ s⁻¹ $^{22-24}$ and ultrahigh photoresponse in the entire visible range.²⁴ Higher electron mobilities of about 70 cm² V⁻¹ s⁻¹ was achieved in TiS₃ nanosheets, too. ²² Scanning tunneling spectroscopy and photoelectrochemical measurements showed that TiS₃ nanoribbons have a band gap of 1.2 eV and an exciton binding energy of 0.13 eV, respectively.²⁵ Applications of TiS₃ as an electrode material for Li batteries²⁶ and for hydrogen generation²⁷ have been investigated.

Due to the large binding energy, excitons are the primary form of photoexcitations and are stable at room temperature. Hence, they are expected to dominate optical responses of TiS₃ nanoribbons. Understanding their properties, especially dynamical properties, is necessary for developing novel optoelectronic applications based on this material. Here we report time and spatially resolved measurement of exciton dynamics in TiS₃ nanoribbons.

2. MATERIALS AND METHODS

The TiS₃ nanoribbons were grown by using a combination of titanium foil of about 0.2 g with excess elemental sulfur of about 0.5 g. The mixture was sealed in a quartz ampule at a pressure of about 200 mTorr and annealed in a furnace at 550 °C for 4 days.

In the transient absorption setup, the 532 nm output of a diode laser was used to pump a Ti:sapphire laser, which generates 150 fs

Received: April 6, 2016 Accepted: June 30, 2016 Published: June 30, 2016

18334

Department of Physics and Astronomy, The University of Kansas, Lawrence, Kansas 66045, United States

^{*}Department of Chemistry and Nebraska Center for Materials and Nanoscience, University of Nebraska - Lincoln, Lincoln, Nebraska 68588. United States

pulses with a central wavelength of 790 nm. A beamsplitter was used to separate it to two beams. By focusing one of the beams to a beta barium borate crystal, we generated its second harmonic at 395 nm, which was used as a pump. The other 790 nm beam was coupled to a photonic crystal fiber to generate supercontinuum. A bandpass filter with a passing wavelength of 950 nm and a bandwidth of 10 nm was employed to select a 950 nm pulse from the supercontinuum, which serve as the probe. A half-wave plate and a polarizer were used to control the polarization and power of each beam. The pump and probe were linearly polarized along perpendicular directions. A dichroic beamsplitter was used to combine the pump and probe beams, which were both focused to the sample by a microscope objective lens. The reflected probe pulse from the sample was sent to a silicon photodetector, which was connected to a lock-in amplifier. The pump pulse was modulated by a mechanical chopper at about 2.2 kHz. The sample was fixed on a 3-dimensional translational stage. With the assistance of an imaging system, the laser spots were located at the central regions of TiS3 nanoribbons to avoid edge effects. All measurements were performed at room temperature.

3. RESULTS AND DISCUSSION

Figure 1 summarizes material characterization of TiS₃ samples. Shiny black TiS3 whiskers were formed both on Ti foil and on

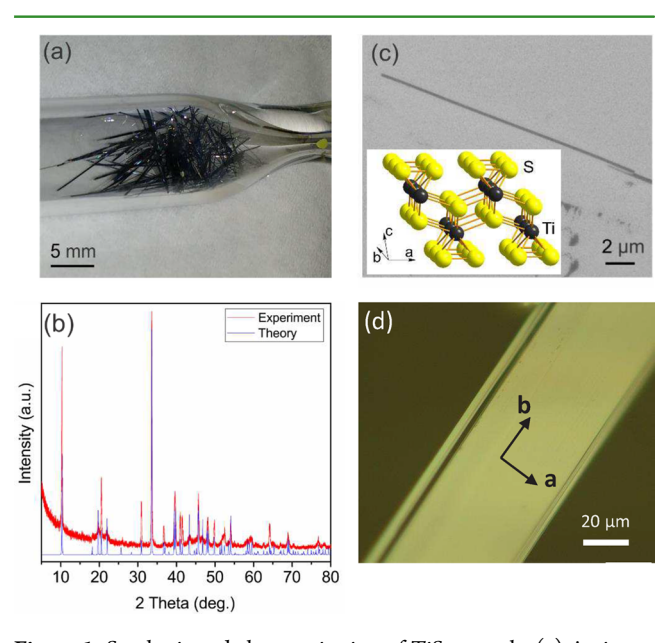


Figure 1. Synthesis and characterization of TiS₃ crystals. (a) A picture of TiS₃ single crystals formed on the walls of a quartz ampule. (b) Powder X-ray diffraction pattern obtained from TiS₃ single crystals (red) and theoretical pattern for TiS₃ phase (blue). (c) Scanning electron microscopy image of a mechanically exfoliated TiS3 crystal on the Si/SiO₂ substrate. The crystal structure of TiS₃ and the principal crystallographic directions are shown in the inset. (d) Optical microscopy image of a TiS₃ nanoribbon along the b direction.

the walls of the ampule, see Figure 1(a). The crystals grown on the walls were isolated and characterized by powder X-ray diffraction, as shown in Figure 1(b). Cell parameters of TiS₃ phase, extracted from the X-ray diffraction pattern, are consistent with those reported earlier (a = 0.4969, b =0.3397, c = 0.8797 nm, and $\beta = 97.23^{\circ}$). The lattice structure and the three principal crystalline directions are illustrated in the inset of Figure 1(c). No signatures from additional phases, such as TiS2 and TiO2, were observed from the X-ray diffraction, which confirms the purity of the sample. For scanning electron microscopy (SEM) characterization, the samples were mechanically exfoliated onto a Si/SiO₂ substrate.

A representative SEM image of an exfoliated TiS₃ nanoribbon, which is less than 1 μ m wide, is shown in Figure 1(c). For optical measurements, we typically used wider nanoribbons to avoid possible edge effects. More detailed material characterization of bulk TiS₃ grown by the described procedure can be found in a previous report.²³

Transient absorption measurements were performed on a number of TiS₃ nanoribbon samples, with similar results obtained. Here, we will present results from one sample shown in Figure 1(d). The thickness of this sample is about 3 μ m, determined by atomic force microscopy measurements (see the Supporting Information). In these measurements, electron hole pairs are excited by a 395 nm (3.14 eV) pump pulse with a time duration of about 200 fs. The dynamics of these photocarriers are monitored by measuring differential reflection of a probe pulse of 950 nm and 300 fs. The differential reflection is defined as the normalized change of the probe reflection induced by the pumps, $\Delta R/R_0 = [R(N) - R_0]/R_0$, where R(N) and R_0 are the reflectance of the probe by the sample with and without the presence of the pump pulse, respectively.

Figure 2 shows the measured differential reflection signal as a function of the probe delay (defined as the lagging time of the

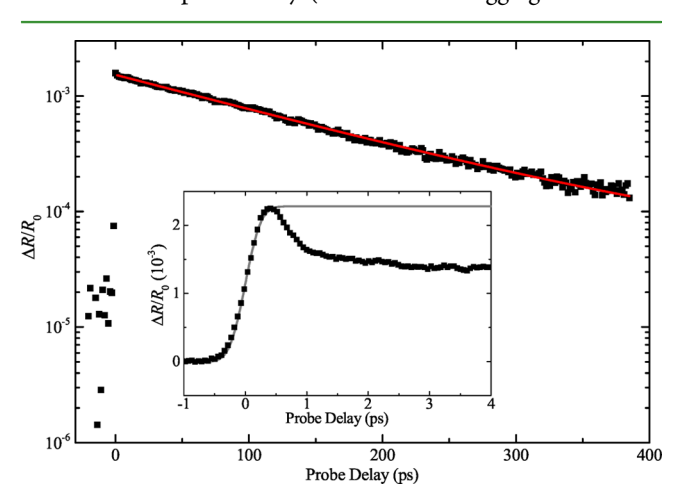


Figure 2. Differential reflection signal of a 950 nm probe pulse as a function of the probe delay after the sample is excited by a 395 nm pump pulse. The red curve is a single-exponential fit with a time constant of 140 ps. The inset shows the signal at early delays. The gray curve is the integral of a Gaussian function with a width of 0.47 ps.

probe pulse with respect to the pump pulse). In this measurement, the pump pulse with an energy fluence of 4 μ J cm⁻² injects a peak photocarrier density (at the center of the pump spot) near the sample surface of about 8×10^{17} cm⁻³ which is estimated by using an absorption coefficient of 1×10^7 m⁻¹ and a reflectance of 0.1 at the pump wavelength.²⁸ As shown in the inset of Figure 2, the differential reflection signal rapidly reaches a peak after the excitation of the pump pulse. The gray curve is the integral of a Gaussian function with a width of 0.47 ps (full width at half-maximum). This is close to the response time of the setup. After a subpicosecond drop, the signal decays single-exponentially, with a time constant of 140 \pm 5 ps, as indicated by the red curve in the main panel of Figure

To understand the observed dynamics, we note that with a band gap of 1.2 eV, 25 the 3.14 eV pump injects electron-hole pairs with excess energies of about 1 eV, while the 1.3 eV probe predominately senses carriers populating states that are about 50 meV above the bandedges and excitons. The electrons and holes are injected with a narrow Gaussian energy distribution, dictated by the spectrum of the pump pulse. This distribution evolves to a Fermi-Dirac distribution in a thermalization process, achieved by exchange of energy among the carrier via carrier-carrier scattering. Then, the hot carriers will relax their energy to reach quasi-equilibrium with the lattice at 300 K. This energy relaxation is achieved by emission of phonons. Both the thermalization and energy relaxation involve movement of carriers into the probing window and hence should cause an increase in the differential reflection signal. The lack of a resolvable rising part of the signal suggests that these processes are completed on a time scale faster than 0.5 ps.

The thermalized and cooled electron-hole pairs are expected to form excitons. Since the exciton binding energy²⁵ of 0.13 eV is much larger than thermal energy at 300 K, once formed, excitons are expected to be stable and decay due to radiative or nonradiative recombination. The small drop right after the peak observed in the inset of Figure 2 could be associated with the exciton formation, since in this process the carriers are moving out of the probing window. The excitons can induce a differential reflection signal for the probe tuned above the bandedge due to the phase-space state filling effect, since the exciton states are formed by superposition of all free carrier states.²⁹ Hence, the occupation of an exciton state influences excitation of other free carrier states. However, if the excitons are less efficient in inducing the signal than free carriers of the same density, the signal is expected to decrease as the free carriers form excitons.

The single-exponential decay of the signal after this fast transient provides further evidence that the exciton formation is a fast process. Otherwise, we would expect a multiexponential decay involving both exciton formation and recombination. The decay constant of 140 ps can then be assigned to the exciton lifetime. Given the rather low photoluminescence yield, this lifetime is likely limited by nonradiative recombinations assisted by defect states, where the exciton recombination results in emission of phonons, instead of photons.

Previously, the density-dependent decay process of transient absorption or photoluminescence signal has been generally observed in TMDs, including $MoS_{\upsilon}^{30,31}$ $MoSe_{\upsilon}^{32}$ WS_{υ}^{33} and WSe₂,³⁴ and was attributed to exciton–exciton annihilation. The single-exponential decay observed in TiS₃ nanoribbons suggests that density-dependent multiexciton processes are absent. To further confirm this observation, we repeat the measurement with various values of the pump pulse fluence, that is, injected carrier density. As shown in Figure 3, the decay of the signal is independent of the pump fluence. The magnitude of the signal is proportional to the pump fluence, as indicated in the inset. With exciton-exciton annihilation, the decay is expected to be faster at higher densities. 30-34

The measurements shown in Figures 2 and 3 were performed with the centers of the focused pump and probe laser spots overlapped. In the following, we study the in-plane transport property of excitons by performing spatially resolved transient absorption measurements. Here, the time-dependent differential reflection signals, such as shown in Figure 2, were measured with different distances between the centers of the pump and probe spots, achieved by tilting the beamsplitter that sends the probe beam to the objective lens.

Figure 4(a) shows the differential reflection signal as a function of both the probe delay and the probe position (the

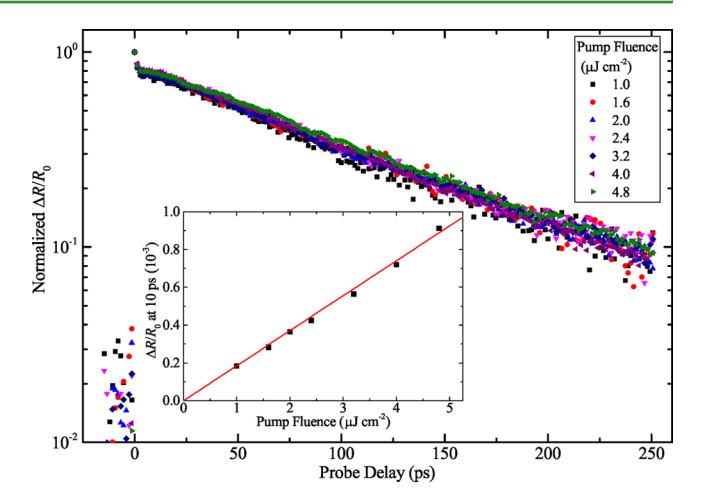


Figure 3. Normalized differential reflection signal of a 950 nm probe pulse as a function of the probe delay after the sample is excited by a 395 nm pump pulse. The values of the pump fluence are indicated in the label. The inset shows the magnitude of the signal, reflected by the signal at a probe delay of 10 ps, as a function of the pump fluence. The red line shows a linear fit.

distance between the centers of the pump and probe spot). Here, the probe spot was scanned along the vertical direction in laboratory coordinate, while the sample is oriented such that the **b** direction is vertical (see Figure 1 for the definition of **b**). At each probe delay, the spatial profile of the difference reflection is proportional to the spatial distribution of the excitons along b. Figure 4(b) shows a few examples of these profiles obtained at several probe delays. By fitting these profiles with a Gaussian function, we deduce the squared width (full width at half-maximum), which is plotted as a function of the probe delay in Figure 4(c).

The broadening of the profile observed in Figure 4(c)originates from diffusion of excitons along b. As shown in Figure 3, decay of the differential reflection signal is independent of the exciton density. Hence, different parts of the profile decay at the same rate, and the exciton recombination only causes reduction of the height of the profile, without changing the width. On the other hand, diffusion of excitons would broaden the profiles. According to the diffusion model, the squared width of the profile is proportional to time, $w^2(t) = w^2(t_0) + 16 \ln(2)D(t-t_0)$, where D is the diffusion coefficient of excitons, and t_0 is an arbitrarily chosen initial time. From a linear fit (red line), we obtain a diffusion coefficient of 1.2 ± 0.2 cm² s⁻¹. To study the exciton diffusion perpendicular to the b direction, the measurement was repeated by scanning the probe spot along the horizontal direction (that is, perpendicular to **b** direction). The results are summarized in Figure 5, similar to Figure 4. A similar exciton diffusion coefficient of 1.0 ± 0.3 cm² s⁻¹ was obtained.

For a thermalized particle system, the diffusion coefficient is related to the mobility, μ , by the Einstein relation, $D/k_{\rm B}T = \mu/e$, where e, $k_{\rm B}$, and T are elementary charge, Boltzmann constant, and the temperature of the distribution. The measured diffusion coefficient corresponds to an exciton mobility of about 50 cm² V^{-1} s⁻¹. Recently, charge mobilities in the range of 20 to 70 cm² V^{-1} s⁻¹ were deduced from transport measurements.^{22–24} Although excitons and charge carriers interact with their environments differently, the order-of-magnitude agreement of these mobilities is satisfactory. Furthermore, by using the

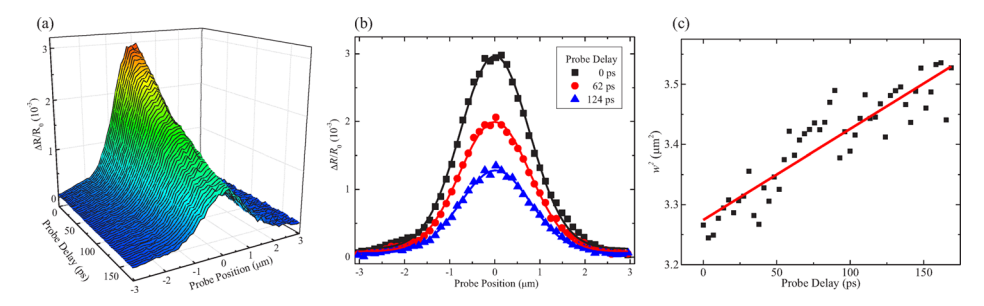


Figure 4. (a) Differential reflection signal as a function of both the probe delay and the probe position, as the probe spot is scanned along b. (b) Spatial profiles at the probe delay of 0, 62, and 124 ps. (c) Squared width of spatial profile as a function of probe delay. The red line is a linear fit.

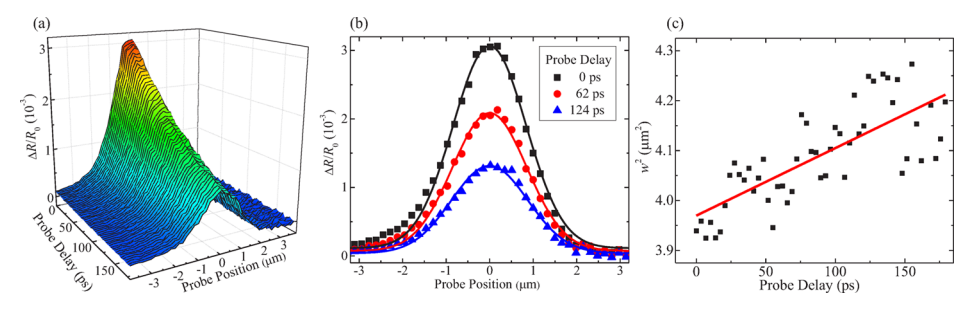


Figure 5. (a) Differential reflection signal as a function of both the probe delay and the probe position, as the probe spot is scanned perpendicular to b. (b) Spatial profiles at the probe delay of 0, 62, and 124 ps. (c) Squared width of spatial profile as a function of probe delay. The red line is a linear fit.

measured exciton lifetime of τ = 140 ps, we deduce an exciton diffusion length of $\sqrt{D\tau}$ = 130 nm.

4. CONCLUSION

We synthesized ${\rm TiS_3}$ nanoribbons and performed transient absorption measurements of photocarrier and exciton dynamics in this newly developed nanomaterial. Time-resolved measurements indicate that following ultrafast injection, the thermalization, energy relaxation, and exciton formation of photocarriers all occur on a subpicosecond time scale. The thermalized exciton population decays with a lifetime of 140 ps, which is attributed to nonradiative recombination of excitons. From spatially and temporally resolved measurements, we deduced an exciton diffusion coefficient of 1.2 cm² s $^{-1}$, a diffusion length of 130 nm, and an exciton mobility of about 50 cm² V $^{-1}$ s $^{-1}$.

ASSOCIATED CONTENT

Supporting Information

The Supporting Information is available free of charge on the ACS Publications website at DOI: 10.1021/acsami.6b04092.

Atomic force microscopy measurement of the sample (PDF)

AUTHOR INFORMATION

Corresponding Authors

*E-mail: sinitskii@unl.edu. *E-mail: huizhao@ku.edu.

Notes

The authors declare no competing financial interest.

ACKNOWLEDGMENTS

H.Z. acknowledges support of the National Science Foundation of USA under award Nos. DMR-1505852 and IIA-1430493.

A.S. and X.C.Z. were supported by the National Science Foundation through the Nebraska Materials Research Science and Engineering Center (MRSEC) with award No. DMR-1420645. A.S. acknowledges support from the National Science Foundation through ECCS-1509874.

REFERENCES

- (1) Mak, K. F.; Lee, C.; Hone, J.; Shan, J.; Heinz, T. F. Atomically Thin MoS_2 : A New Direct-Gap Semiconductor. *Phys. Rev. Lett.* **2010**, 105. 136805.
- (2) Splendiani, A.; Sun, L.; Zhang, Y.; Li, T.; Kim, J.; Chim, C. Y.; Galli, G.; Wang, F. Emerging Photoluminescence in Monolayer MoS₂. *Nano Lett.* **2010**, *10*, 1271–1275.
- (3) Xiao, D.; Liu, G. B.; Feng, W.; Xu, X.; Yao, W. Coupled Spin and Valley Physics in Monolayers of MoS₂ and Other Group-VI Dichalcogenides. *Phys. Rev. Lett.* **2012**, *108*, 196802.
- (4) Zeng, H.; Dai, J.; Yao, W.; Xiao, D.; Cui, X. Valley Polarization in MoS₂ Monolayers by Optical Pumping. *Nat. Nanotechnol.* **2012**, *7*, 490–493.
- (5) Mak, K. F.; He, K.; Shan, J.; Heinz, T. F. Control of Valley Polarization in Monolayer MoS₂ by Optical Helicity. *Nat. Nanotechnol.* **2012**, *7*, 494–498.
- (6) Mak, K. F.; He, K.; Lee, C.; Lee, G. H.; Hone, J.; Heinz, T. F.; Shan, J. Tightly Bound Trion in Monolayer MoS₂. *Nat. Mater.* **2013**, *12*, 207–211.
- (7) Ross, J. S.; Wu, S.; Yu, H.; Ghimire, N. J.; Jones, A. M.; Aivazian, G.; Yan, J.; Mandrus, D. G.; Xiao, D.; Yao, W.; Xu, X. Electrical Control of Neutral and Charged Excitons in a Monolayer Semiconductor. *Nat. Commun.* **2013**, *4*, 1474.
- (8) Chernikov, A.; Berkelbach, T. C.; Hill, H. M.; Rigosi, A.; Li, Y. L.; Aslan, O. B.; Reichman, D. R.; Hybertsen, M. S.; Heinz, T. F. Exciton Binding Energy and Nonhydrogenic Rydberg Series in Monolayer WS₂. *Phys. Rev. Lett.* **2014**, *113*, 076802.
- (9) He, K.; Kumar, N.; Zhao, L.; Wang, Z.; Mak, K. F.; Zhao, H.; Shan, J. Tightly Bound Excitons in Monolayer WSe₂. *Phys. Rev. Lett.* **2014**, *113*, 026803.
- (10) Zeng, H.; Liu, G.-B.; Dai, J.; Yan, Y.; Zhu, B.; He, R.; Xie, L.; Xu, S.; Chen, X.; Yao, W.; Cui, X. Optical Signature of Symmetry

- Variations and Spin-Valley Coupling in Atomically Thin Tungsten Dichalcogenides. Sci. Rep. 2013, 3, 1608.
- (11) Kumar, N.; Najmaei, S.; Cui, Q.; Ceballos, F.; Ajayan, P. M.; Lou, J.; Zhao, H. Second Harmonic Microscopy of Monolayer MoS₂. *Phys. Rev. B: Condens. Matter Mater. Phys.* **2013**, 87, 161403.
- (12) Malard, L. M.; Alencar, T. V.; Barboza, A. P. M.; Mak, K. F.; de Paula, A. M. Observation of Intense Second Harmonic Generation from MoS₂ Atomic Crystals. *Phys. Rev. B: Condens. Matter Mater. Phys.* **2013**, *87*, 201401.
- (13) Li, Y.; Rao, Y.; Mak, K. F.; You, Y.; Wang, S.; Dean, C. R.; Heinz, T. F. Probing Symmetry Properties of Few-Layer MoS₂ and h-BN by Optical Second-Harmonic Generation. *Nano Lett.* **2013**, *13*, 3329–3333.
- (14) Yin, X.; Ye, Z.; Chenet, D. A.; Ye, Y.; O'Brien, K.; Hone, J. C.; Zhang, X. Edge Nonlinear Optics on a MoS₂ Atomic Monolayer. *Science* **2014**, 344, 488–490.
- (15) Geim, A. K.; Grigorieva, I. V. Van der Waals Heterostructures. *Nature* **2013**, *499*, 419–425.
- (16) Britnell, L.; Ribeiro, R. M.; Eckmann, A.; Jalil, R.; Belle, B. D.; Mishchenko, A.; Kim, Y.-J.; Gorbachev, R. V.; Georgiou, T.; Morozov, S. V.; Grigorenko, A. N.; Geim, A. K.; Casiraghi, C.; Neto, A. H. C.; Novoselov, K. S. Strong Light-Matter Interactions in Heterostructures of Atomically Thin Films. *Science* **2013**, *340*, 1311–1314.
- (17) Britnell, L.; Gorbachev, R. V.; Jalil, R.; Belle, B. D.; Schedin, F.; Mishchenko, A.; Georgiou, T.; Katsnelson, M. I.; Eaves, L.; Morozov, S. V.; Peres, N. M. R.; Leist, J.; Geim, A. K.; Novoselov, K. S.; Ponomarenko, L. A. Field-Effect Tunneling Transistor Based on Vertical Graphene Heterostructures. *Science* **2012**, *335*, 947–950.
- (18) Dai, J.; Li, M.; Zeng, X. C. Group IVB transition metal trichalcogenides: a new class of 2D layered materials beyond graphene. *Wiley Interdiscip. Rev.: Comput. Mol. Sci.* **2016**, *6*, 211–222.
- (19) Dai, J.; Ženg, X. C. Titanium Trisulfide Monolayer: Theoretical Prediction of a New Direct-Gap Semiconductor with High and Anisotropic Carrier Mobility. *Angew. Chem., Int. Ed.* **2015**, *54*, 7572–7576
- (20) Li, M.; Dai, J.; Zeng, X. C. Tuning the Electronic Properties of Transition-Metal Trichalcogenides Via Tensile Strain. *Nanoscale* **2015**, 7, 15385–15391.
- (21) Kang, J.; Sahin, H.; Ozaydin, H. D.; Senger, R. T.; Peeters, F. M. TiS₃ Nanoribbons: Width-Independent Band Gap and Strain-Tunable Electronic Properties. *Phys. Rev. B: Condens. Matter Mater. Phys.* **2015**, 92, 075413.
- (22) Island, J. O.; Barawi, M.; Biele, R.; Almazan, A.; Clamagirand, J. M.; Ares, J. R.; Sanchez, C.; van der Zant, H. S. J.; Alvarez, J. V.; D'Agosta, R.; Ferrer, I. J.; Castellanos-Gomez, A. TiS₃ Transistors with Tailored Morphology and Electrical Properties. *Adv. Mater.* **2015**, 27, 2595–2601.
- (23) Lipatov, A.; Wilson, P. M.; Shekhirev, M.; Teeter, J. D.; Netusil, R.; Sinitskii, A. Few-Layered Titanium Trisulfide (TiS₃) Field-Effect Transistors. *Nanoscale* **2015**, *7*, 12291–12296.
- (24) Island, J. O.; Buscema, M.; Barawi, M.; Clamagirand, J. M.; Ares, J. R.; Sanchez, C.; Ferrer, I. J.; Steele, G. A.; van der Zant, H. S. J.; Castellanos-Gomez, A. Ultrahigh Photoresponse of Few-Layer TiS₂ Nanoribbon Transistors. *Adv. Opt. Mater.* **2014**, *2*, 641–645.
- (25) Molina-Mendoza, A. J.; Barawi, M.; Biele, R.; Flores, E.; Ares, J. R.; Sanchez, C.; Rubio-Bollinger, G.; Agrait, N.; D'Agosta, R.; Ferrer, I. J.; Castellanos-Gomez, A. Electronic Bandgap and Exciton Binding Energy of Layered Semiconductor TiS₃. *Adv. Electron. Mater.* **2015**, *1*, 1500126.
- (26) Hayashi, A.; Matsuyama, T.; Sakuda, A.; Tatsumisago, M. Amorphous Titanium Sulfide Electrode for All-Solid-State Rechargeable Lithium Batteries with High Capacity. *Chem. Lett.* **2012**, *41*, 886–888.
- (27) Barawi, M.; Flores, E.; Ferrer, I. J.; Ares, J. R.; Sanchez, C. Titanium Trisulphide (TiS₃) Nanoribbons for Easy Hydrogen Photogeneration under Visible Light. *J. Mater. Chem. A* **2015**, 3, 7959–7965.

- (28) Ferrer, I. J.; Ares, J. R.; Clamagirand, J. M.; Barawi, M.; Sanchez, C. Optical Properties of Titanium Trisulphide (TiS₃) Thin Films. *Thin Solid Films* **2013**, 535, 398–401.
- (29) Schmitt-Rink, S.; Chemla, D. S.; Miller, D. A. B. Theory of Transient Excitonic Optical Nonlinearities in Semiconductor Quantum-Well Structures. *Phys. Rev. B: Condens. Matter Mater. Phys.* **1985**, 32, 6601–6609.
- (30) Sun, D.; Rao, Y.; Reider, G. A.; Chen, G.; You, Y.; Brezin, L.; Harutyunyan, A. R.; Heinz, T. F. Observation of Rapid Exciton-Exciton Annihilation in Monolayer Molybdenum Disulfide. *Nano Lett.* **2014**, *14*, 5625–5629.
- (31) Kar, S.; Su, Y.; Nair, R. R.; Sood, A. K. Probing Photoexcited Carriers in a Few-Layer MoS₂ Laminate by Time-Resolved Optical Pump-Terahertz Probe Spectroscopy. *ACS Nano* **2015**, *9*, 12004–12010.
- (32) Kumar, N.; Cui, Q.; Ceballos, F.; He, D.; Wang, Y.; Zhao, H. Exciton-Exciton Annihilation in MoSe₂ Monolayers. *Phys. Rev. B: Condens. Matter Mater. Phys.* **2014**, 89, 125427.
- (33) Yuan, L.; Huang, L. B. Exciton Dynamics and Annihilation in WS₂ 2D Semiconductors. *Nanoscale* **2015**, *7*, 7402–7408.
- (34) Mouri, S.; Miyauchi, Y.; Toh, M.; Zhao, W.; Eda, G.; Matsuda, K. Nonlinear Photoluminescence in Atomically Thin Layered WSe₂ arising from Diffusion-Assisted Exciton-Exciton Annihilation. *Phys. Rev. B: Condens. Matter Mater. Phys.* **2014**, *90*, 155449.